

## Full Length Article

# Physics-based and data-driven hybrid modelling and optimisation of stirred-slurry reactors for CO<sub>2</sub> capture via enhanced weathering of dolomite mineral



Yalun Zhao<sup>a</sup>, Mingliang Wang<sup>b</sup>, Jin Xuan<sup>c</sup>, Dengao Chang<sup>a</sup>, Ziming Li<sup>a</sup>, Shiyu Wang<sup>a</sup>, Yun Ou<sup>a</sup>, Xu Wang<sup>a,\*</sup>, Lei Xing<sup>c,\*</sup>

<sup>a</sup> School of Resources and Environmental Sciences, Hubei International Scientific and Technological Cooperation Base of Sustainable Resource and Energy, Wuhan University, Wuhan 430079, China

<sup>b</sup> China communications construction Co. Ltd., Beijing 100088, China

<sup>c</sup> School of Chemistry and Chemical Engineering, Faculty of Engineering and Physical Sciences, University of Surrey, Guildford GU2 7XH, United Kingdom

## ARTICLE INFO

**Keywords:**

Enhanced weathering  
CO<sub>2</sub> capture  
Stirred-slurry reactor  
Surrogate model  
Multi-objective optimisation

## ABSTRACT

The natural enhanced weathering (EW) must be significantly accelerated by optimizing the local triple-phase environment prior to practical large-scale carbon dioxide removal (CDR). The implementation of stirred-slurry reactor (SSR) for enhancing mass transport and reaction rates of the EW-based CO<sub>2</sub> capture process has not yet been reported. We conducted a hybrid modelling approach, in which mechanistic and data-driven models are integrated, for the scaled-up batch SSRs designed for EW-based CO<sub>2</sub> capture. It is revealed that CO<sub>2</sub> mass transport into the aqueous phase has significant impact on the overall capture performance. The scaled-up batch system is found to perform comparably to the continuous system in terms of CO<sub>2</sub> capture rate, energy and water consumption. The energy consumption for gas enrichment in the batch system is expected to be less than 50% of that in continuous systems. Multi-objective optimisation reveals the efficacy and accuracy of the hybrid modeling within low energy consumption ranges.

## 1. Introduction

Global greenhouse gas (GHG) emissions, especially carbon dioxide (CO<sub>2</sub>), are rising to unprecedented levels, exacerbating global warming (Adhikari et al., 2023; Prabhakar and Bandyopadhyay, 2023). At the current emission rate, there is an estimated shortfall of 1.2 billion tonnes of CO<sub>2</sub> equivalent in achieving the climate target outlined in the Paris Agreement, even if all mitigation measures are fully implemented (Reershemius et al., 2023). Consensus exists that more actions are crucial to stabilise the climate and limit global temperature rise to well below 2 °C (Danckwerts, 1995; Feng and Hicks, 2023; Terlouw et al., 2021). In 2020, the U.S. Congress legislated specific carbon dioxide removal (CDR) methods, including enhanced weathering (EW) (Fuhrman et al., 2023), to meet climate goals (Prado and Mac Dowell, 2023). Large-scale CDR technologies are projected to offset over 100 billion tonnes of GHGs (Powis et al., 2023), throughout the 21st century, helping to mitigate the ongoing accumulation of atmospheric greenhouse gases (Goll et al., 2021). Approximately 100 million tons of atmospheric CO<sub>2</sub> are naturally absorbed and stored in surface seawater through weathering of rocks annually, eventually precipitating to

form minerals that are safely stored for hundreds of thousands of years (Renforth, 2019). However, slowing the increase in excess CO<sub>2</sub> emissions passively is insufficient (Taylor et al., 2016). EW is a CDR technique that leverages the natural reactions described above (Feng and Hicks, 2023; Lefebvre et al., 2019). This process is designed to enhance the rock's natural capacity to capture CO<sub>2</sub> from the atmosphere and convert it into bicarbonate and small amounts of carbonate through reacting with cations released during rock dissolution. Previously, EW-based strategies for atmospheric CO<sub>2</sub> removal have been demonstrated to be reliable and economic feasible (Beerling et al., 2020; Kantzas et al., 2022; Jiang et al. 2023).

Techniques aimed at reducing rock particle size to enhance specific areas through comminution and utilising stirring to enhance mineral dissolution in the EW process have been proven feasible (Hangx and Spiers, 2009; Moosdorff et al., 2014), potentially accelerating the reaction rate by a fold of 100 or more (Foteinis et al., 2023). However, the current technologies for EW have only advanced to desktop techno-economic assessments and experimental laboratory scales (Renforth and Henderson, 2017). Integrating mineral weathering with engineered equipment to enhance the 'natural' processes through chem-

\* Corresponding authors.

E-mail addresses: [xu.wang@whu.edu.cn](mailto:xu.wang@whu.edu.cn) (X. Wang), [l.xing@surrey.ac.uk](mailto:l.xing@surrey.ac.uk) (L. Xing).

ical contactors presents a viable option for scaling up to industrial levels (Rau, 2011; Xing et al., 2021). Previous studies have leveraged the weathering of calcite and limestone to convert CO<sub>2</sub> into bicarbonate in chemical reactors. In this process, CO<sub>2</sub> dissolves in an aqueous environment and reacts with OH<sup>-</sup> ions from the weakly alkaline solution produced by mineral dissolution, forming bicarbonate as expressed by the reaction: CO<sub>2(aq)</sub> + OH<sup>-</sup> = HCO<sub>3</sub><sup>-</sup> (Xing et al., 2021). Based on these findings, mathematical modeling has been conducted for both trickle-bed reactor (TBR) (Xing et al., 2021) and packed bubble column (PBC) (Xing et al., 2022) systems. While this approach is a rational choice for implementing EW, the two minerals and reactor types appear to be underrepresented (Hartmann et al., 2013; Renforth and Henderson, 2017). To the best of the authors' knowledge, there are currently no publications on the application of stirred-slurry reactor (SSR) for EW-based CO<sub>2</sub> capture although SSRs are effective in significantly improving particle dissolution (Bin, 1984) and enhancing gas-liquid mass transfer (Lekhal et al., 1997).

In this work, we extended our focus to dolomite, a mineral previously identified by Busenberg and Plummer (1982) and Renforth (2012) as having significant potential for CO<sub>2</sub> capture. We explored its application in a stirred system in addition to fixed bed systems, e.g., trickle bed and packed bubble column (Xing et al., 2021, 2022; Zhang et al., 2023), while also evaluating energy and water consumptions as additional performance indicators. Furthermore, we designed and experimentally validated a pilot-scale SSR to investigate the impact of design variables on key performance indicators. Traditionally, determining the optimal solution through exhaustive search is cumbersome and the interactive effects between variables are difficult to discern (Bezerra et al., 2008). Therefore, a more efficient method is needed to calculate the Pareto frontier for multi-objective optimisation (Xing et al., 2023a). Response Surface Methodology (RSM) is suitable for describing relationships between multiple independent variables and dependent objectives, providing a mathematical technique that significantly reduces the time and resources required for computations (Witek-Krowiak et al., 2014). Leveraging this, we developed a data-driven surrogate model based on RSM for rapid multi-objective prediction and optimisation. It has been

demonstrated that CO<sub>2</sub> capture is more effective when utilising concentrated CO<sub>2</sub> and fresh water (Xing et al., 2022). However, this approach can be costly (Jiang et al., 2023). Batch processing technology has the advantage of improving freshwater utilisation (Chen and Lee, 2010), while its enclosed environment contributes to reducing the energy required for gas enrichment, making it a suitable option. When using smaller particle sizes, SSR appear to be particularly appropriate (Iliuta and Larachi, 2012).

This work examines the effect of EW using SSR on dolomite, incorporating experimental validation at the laboratory scale and the development of a comprehensive mathematical model. Considering the reaction's complexity, operational parameters such as temperature (Oelkers et al., 2018) in the batch system were analyzed in the amplification scenario, and resource consumption throughout the process was assessed. A data-driven surrogate model was developed using response surface methodology (RSM) (Xing et al., 2023b). Optimised outcomes were achieved by refining five operating conditions, i.e., particle diameter ( $d_p$ ), particle loading ( $m_p$ ), liquid-to-gas volume ratio ( $L/G$ ), gas flow rate ( $Q_G$ ) and CO<sub>2</sub> inlet concentration ( $x_{CO_2}$ ), to meet three primary objectives: maximising CO<sub>2</sub> capture rate (CCR), minimising water consumption (WC), and reducing specific energy consumption (SEC). The technical feasibility of industrial application was also evaluated by simulating a gas mixture with a 15% CO<sub>2</sub> mole fraction.

## 2. Experimental procedures and materials

As shown in Fig. 1, the experiment was conducted in a specially designed SSR reactor with a reaction chamber volume of 14 liters, tailored for EW-based CO<sub>2</sub> capture processes. Detailed information on the reactor dimensions and operational equipment can be found in the Supporting Information (SI). Pumps were used to facilitate countercurrent circulation of liquid and gas within the reactor, ensuring thorough mixing of the solution. Additionally, a motor-driven paddle stirred the particles to maintain a homogeneous suspension system. Throughout the reaction process, the reactor's internal space was isolated from the external environment and the volume of the liquid within the reactor was

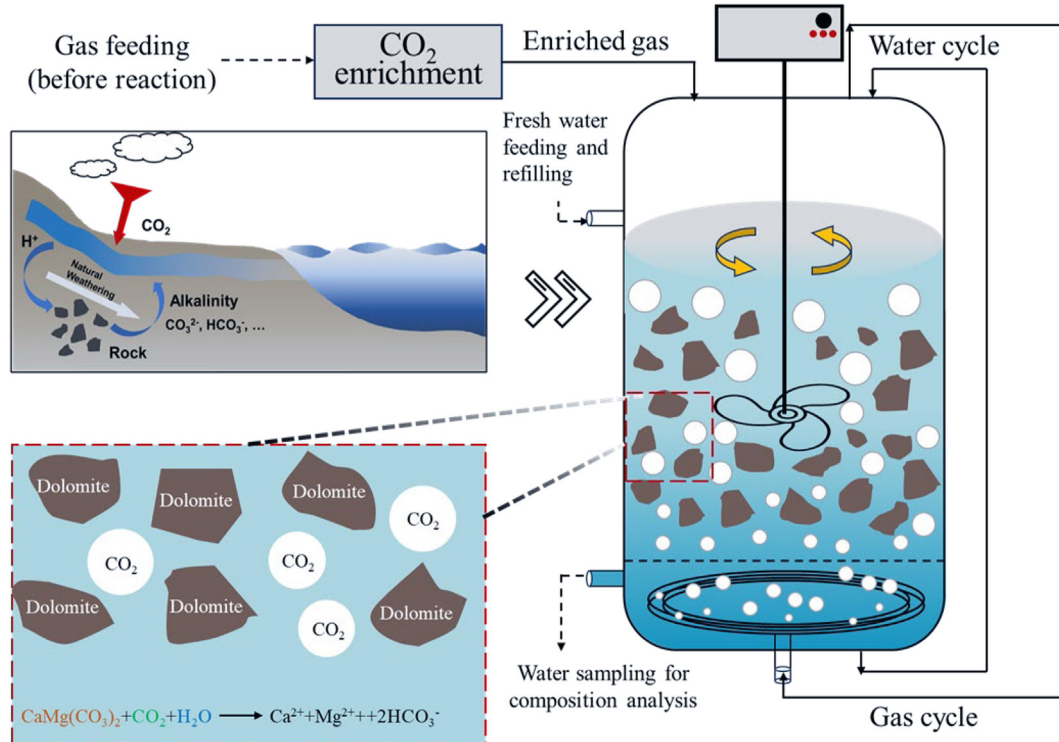


Fig. 1. EW-based CO<sub>2</sub> capture mechanism in a stirred-slurry reactor.

maintained at a constant. The headspace of the SSR was maintained at 1 atm, and the CO<sub>2</sub> concentration was continuously monitored using a Gem Scientific G110 infrared CO<sub>2</sub> analyser. To minimise the impact of volume changes on alkalinity measurements during sampling, the water inside the reactor was replenished using water from a parallel system operating under identical conditions. It is crucial to emphasise that the liquid-to-gas volume ratio (*L/G*), determined prior to each experiment, refers to the ratio of the volumes of liquid and gas in the available space remaining after subtracting the volume occupied by the mineral particles from the total internal volume of the chamber. Dolomite particles measuring 0.4 mm were selected for this study, the properties of the particles are detailed in Section S2 of SI (Fig. S1-S4, Table S1).

### 3. Model development

A physics-based model for a batch SSR was developed. The solid-liquid mixture was treated as a homogeneous phase without considering the uniform spatial distribution of solid particle when stirring. The gas functions as a discrete phase, with gas bubbles traversing the solid-liquid mixing zone. The model incorporated the dissolution kinetics of dolomite and the mass transport of CO<sub>2</sub> bubbles into aqueous phase, which was validated by the designated experiments at various operating conditions. As illustrated in Fig. 2, within the reactor, the gas mixture and liquid are continuously circulated. Gas-liquid mass transfer occurs at the bubble-liquid interface, resulting in a decrease in CO<sub>2</sub> concentration in the headspace of the reactor.

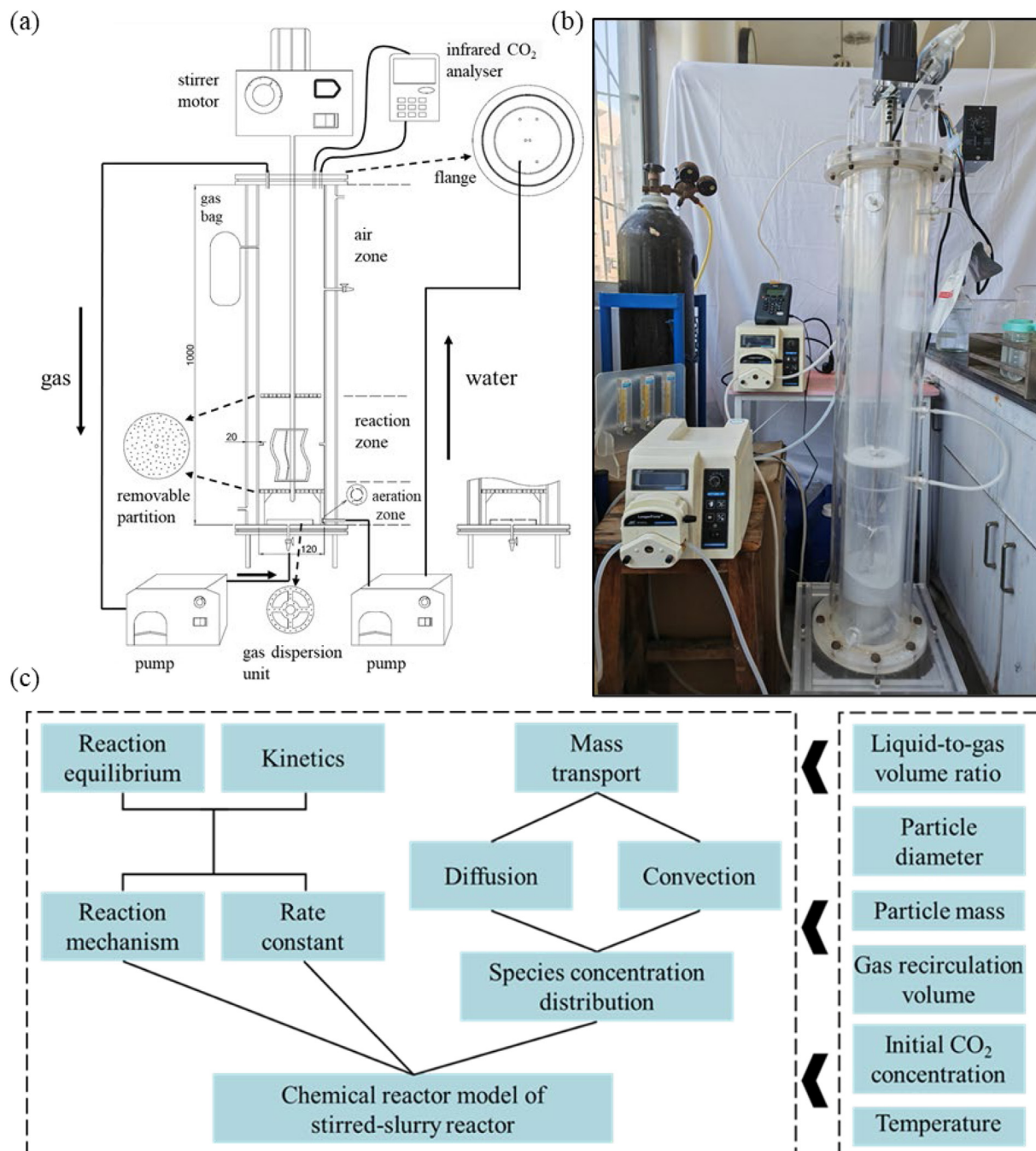


Fig. 2. (a) Schematic diagram, (b) experimental setup, and (c) mechanistic model framework of the SSR reactor.

**Table 1**  
Rate constants and equilibrium constants in the model.

Parameter	Value	Unit	Reference
$K_1$	$K_4/K_W$	$\text{m}^3 \text{ mol}^{-1}$	Calculated
$K_2$	$10^{(1568.9/T - 2.5866 - 6.737 \times 10^{-3}T)}$	$\text{m}^3 \text{ mol}^{-1}$	(Cents et al., 2005; Hikita et al., 1976)
$K_3$	$1/K_W$	$\text{m}^6 \text{ mol}^2$	Calculated
$K_4$	$\rho_w \exp(-12.0921/T - 36.7816 \ln T + 235.482)$	$\text{mol}^{-3}$	(Edwards et al., 1978)
$K_5$	$K_{sp}/(K_2 K_W)^2$	$\text{mol}^2 \text{ m}^{-6}$	Calculated
$K_6$	$K_{sp}(K_4)^2/(K_2 K_W)^2$	$\text{mol}^4 \text{ m}^{-12}$	Calculated
$K_7$	$K_{sp}/(K_2)^2$	$\text{mol}^6 \text{ m}^{-18}$	Calculated
$k_{51}$	$10^{(2.12 - 1880/T)}$	$\text{cm}^{0.5} \text{ mol}^{0.5} \text{ s}^{-1}$	(Busenberg and Plummer, 1982)
$k_{61}$	$10^{(-0.07 - 1800/T)}$	$\text{cm}^{0.5} \text{ mol}^{0.5} \text{ s}^{-1}$	(Busenberg and Plummer, 1982)
$k_{71}$	$10^{(0.53 - 2700/T)}$	$\text{cm}^{0.5} \text{ mol}^{0.5} \text{ s}^{-1}$	(Busenberg and Plummer, 1982)
$K_{sp}$	$10^{(17.502 - 4220.119/T - 0.0689T)}$	$\text{mol}^4 \text{ L}^{-4}$	(Bénézeth et al., 2018)
$K_W$	$\rho_w^2 10^{(-5839.50/T - 22.4773 \log T + 61.2062)}$	$\text{mol}^2 \text{ m}^{-6}$	(Tsonopoulos et al., 1976)

Note:  $T$  (K) is the reaction temperature.

The developed model integrates the kinetics of dolomite particle dissolution within the water- $\text{CO}_2$  system alongside  $\text{CO}_2$  mass transfer processes. The following assumptions were made:

- (1) Each batch runs for two hours as the reaction nears equilibrium.
- (2) No additional particles were introduced into the reactor throughout the entire reaction.
- (3) Radial concentration gradients of species were not considered.
- (4) The reactant gas comprised a mixture of carbon dioxide and nitrogen, with no other gaseous impurities influencing the reaction kinetics.

### 3.1. Reaction kinetics

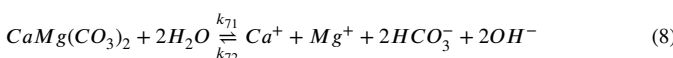
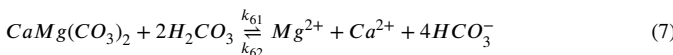
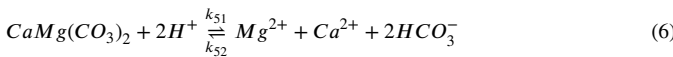
The reaction between  $\text{CO}_2$  and water is essential for the dissolution of minerals in aqueous solutions. The reactions occurring in the aqueous phase are as follows:



Busenberg and Plummer (1982) identified two principal phases of dolomite dissolution. Initially, a brief non-stoichiometric dissolution phase occurs, during which  $\text{CaCO}_3$  is released from the fresh dolomite surface more rapidly than  $\text{MgCO}_3$ , leading to a surface enrichment of  $\text{MgCO}_3$ . The subsequent and more significant phase involves the stoichiometric release of both solid components (Pokrovsky and Schott, 2001). Overall, the total dissolution rate of dolomite can be estimated by:

$$R = k_1 a_{\text{H}^+}^n + k_2 a_{\text{H}_2\text{CO}_3}^p + k_3 a_{\text{H}_2\text{O}}^{0.5} - k_4 a_{\text{HCO}_3^-} \quad (5)$$

In this equation, the exponent  $n$  is 0.5 up to 45 °C but increases with temperature to a maximum of 0.75, while  $p$  ranges from 0.5 to 1 (Chou et al., 1989). The net stoichiometry of dolomite dissolution in the  $\text{CO}_2\text{-H}_2\text{O}$  system, dependent on the forward reaction rate, can be expressed by the following equation:



The reaction rate constants and equilibrium constants from the above equations are presented in Table 1.

Although the Ca/Mg ratio released during the initial surface dissolution of fresh dolomite is non-stoichiometric, it affects only about 1 to 2 atomic layers (Busenberg and Plummer, 1982). Following this initial phase, the Ca/Mg molar ratio of the released ions becomes stoichiometric and approximates that of the solid itself, whereas the present study shows an atomic ratio of approximately 1:1 (Table S2). When neglecting  $\text{Mg}^{2+}$  and  $\text{Ca}^{2+}$  interactions, the dissolution rates of dolomite and total carbon ions (TCI) can be expressed as:

$$r_{\text{CO}_2(aq)} = r_{G-L} + \epsilon_L \left( k_{12} c_{\text{HCO}_3^-} - k_{11} c_{\text{CO}_2(aq)} c_{\text{OH}^-} + k_{42} c_{\text{HCO}_3^-} c_{\text{H}^+} - k_{41} c_{\text{CO}_2(aq)} \right) + a_s \left( k_{62} c_{\text{Ca}^{2+}} c_{\text{Mg}^{2+}} c_{\text{HCO}_3^-}^4 - k_{61} c_{\text{CO}_2(aq)}^2 \right) \quad (9)$$

$$r_{\text{Me}^{2+}} = a_s \left[ k_{51} c_{\text{H}^+}^2 - k_{52} c_{\text{Ca}^{2+}} c_{\text{Mg}^{2+}} c_{\text{HCO}_3^-}^2 + k_{61} c_{\text{CO}_2(aq)}^2 - k_{62} c_{\text{Ca}^{2+}} c_{\text{Mg}^{2+}} c_{\text{HCO}_3^-}^4 + k_{71} - k_{72} c_{\text{Ca}^{2+}} c_{\text{Mg}^{2+}} c_{\text{HCO}_3^-}^2 c_{\text{OH}^-} \right] \quad (10)$$

$$r_{\text{TCI}} = -\epsilon_L \left[ k_{12} c_{\text{HCO}_3^-} - k_{11} c_{\text{CO}_2(aq)} c_{\text{OH}^-} + k_{42} c_{\text{HCO}_3^-} c_{\text{H}^+} - k_{41} c_{\text{CO}_2(aq)} \right] + r_{\text{Me}^{2+}} \quad (11)$$

where  $\text{Me}^{2+}$  represents  $\text{Ca}^{2+}$  and  $\text{Mg}^{2+}$ ,  $a_s$  ( $\text{m}^{-1}$ ) denotes the total solid-liquid interfacial area, which can be derived using the following expression (Benyahia and O'Neill, 2005):

$$a_s = 6(1 - \epsilon)/d_p \quad (12)$$

where  $\epsilon$  (-) is the porosity of the solid bed before filled with liquid and gas, derivable from the following expression:

$$\epsilon = 0.390 + \frac{1.740}{(d_r/d_p + 1.14)^2} \quad (13)$$

where  $d_r$  (m) is the internal diameter of the reactor and  $\epsilon_S$  is related to  $\epsilon$  as:

$$\epsilon_S = 1 - \epsilon \quad (14)$$

The following equation applies to SSR:

$$\epsilon_S + \epsilon_L + \epsilon_G = 1 \quad (15)$$

where  $\epsilon_i$  (-) is the proportion of component  $i$  to the total bed, the gas hold up,  $\epsilon_G$  (-), is given by the following equation (Darton, 1985):

$$\epsilon_G = \frac{1}{8} \ln \left[ 1 + 8Cg^{-7/24} \left( \frac{\mu_c}{\rho_c} \right)^{-1/6} \left( \frac{\sigma}{\rho_c} \right)^{-1/8} U_g \right] \quad (16)$$

where  $C$  is a constant, with  $C = 0.2$  for the stirred turbulent system.,  $\mu_c$  ( $\text{Pa s}$ ),  $\rho_c$  ( $\text{kg m}^{-3}$ ) and  $\sigma$  ( $\text{N m}^{-1}$ ) are the viscosity, density, and surface tension of the continuous phase, respectively,  $U_g$  ( $\text{m s}^{-1}$ ) is the superficial velocity of the gas.

$$U_g = 4Q_g/\pi d_r^2 \quad (17)$$

### 3.2. Mass transfer and phase fractions

In the SSR system, the equation describing the variation of CO<sub>2</sub> concentration in the gas phase is nearly identical to that of the packed bubble column system. The mass transfer coefficients for the liquid and gas phases in a three-phase system are given as follows (Akita and Yoshida, 1973):

$$K_L = 0.5g^{5/8}(d_b E_L)^{1/2}(\sigma/\rho_c)^{-3/8} \quad (18)$$

$$K_G = 5.23 \left( \frac{\rho_G U_G}{a_t \mu_G} \right)^{0.7} \left( \frac{\mu_G}{\rho_G D_{G,m}} \right)^{1/3} (a_t d_p)^{-2.0} a_t D_G \quad (19)$$

where  $D_{G,m}$  (m<sup>2</sup> s<sup>-1</sup>) is the molecular diffusivity of CO<sub>2</sub> in a gas and  $K_H$  is the Henry's coefficient in fresh water, which is expressed as

$$K_H = \frac{1}{\rho_c} \exp^{-6789.04/(T-11.4519 \log T - 0.010454T + 94.491)} \quad (20)$$

The bubble diameter  $d_b$  (m) is obtained from the empirical equation derived by Darton and Harrison (1985) for three-phase slurry bed conditions:

$$d_b = 0.72(\mu_B/\rho_B)^{0.22} U_g^{0.33} \quad (21)$$

In the above equation,  $\mu_B$  (Pa s) is the effective bed viscosity (Du et al., 2023).

$$\mu_B = \mu_c \left( 1 + \frac{5}{2}\varphi + \frac{109}{14}\varphi^2 \right) \quad (22)$$

The parameter  $\varphi$  (-) typically represents the volume fraction of solid particles in the solid-liquid mixture, without considering the volume of gas, and is determined by the following equation:

$$\varphi = \frac{V_p}{V_l + V_p} \quad (23)$$

For the mixed bed,  $V_p$  (m<sup>3</sup>) and  $V_l$  (m<sup>3</sup>) refer to the volume of solid particles and liquid in the reactor, respectively.  $\rho_B$  (kg m<sup>-3</sup>) is the average bed density and can be calculated by the following expression:

$$\rho_B = \rho_p \varphi + \rho_c (1 - \varphi) \quad (24)$$

In the liquid phase, the equation for the variation of liquid substance  $i$  in the reactor is described as follows:

$$\varepsilon_L \frac{\partial}{\partial t} c_i - \varepsilon_L E_L \nabla^2 c_i + u_L \nabla \cdot c_i = r_i \quad (25)$$

where  $C_i$  (mol m<sup>-3</sup>) is the concentration of a particular substance  $i$  in the liquid, with  $i$  referring to CO<sub>2</sub>, metal cations and total carbon ions in the solution,  $u_L$  (m s<sup>-1</sup>) denotes the superficial velocity of the liquid, and  $r_i$  (mol m<sup>-3</sup> s<sup>-1</sup>) is the source term for substance  $i$ ,  $E_L$  (m<sup>2</sup> s<sup>-1</sup>) is the longitudinal dispersion coefficient, which can be calculated using the following expression (Darton, 1985).

$$E_L = 0.43d_r^{4/3}[(U_g - \varepsilon_{g,l} U_{b\infty})g]^{1/3} \quad (26)$$

where  $\varepsilon_{g,l}$  (-) is the gas content of the gas-liquid system, which can be corrected according to the following equation:

$$\varepsilon_G/\varepsilon_{g,l} = (\rho_L/\rho_B)^{1.22} \quad (27)$$

The bubble rise rate  $U_b$  (m s<sup>-1</sup>) can be obtained by the following equation:

$$U_b = U_g + U_{b\infty} \quad (28)$$

where  $U_{b\infty}$  (m s<sup>-1</sup>) is the rising velocity of an independent bubble in a stagnant liquid:

$$U_{b\infty} = 22.3 \left[ \frac{V_b}{10^6} \right]^{1/6} \quad (29)$$

where  $V_b$  (m<sup>3</sup>) is the single bubble volume, which can be obtained from  $d_b$  as:

$$V_b = \frac{\pi d_b^3}{6} \quad (30)$$

**Table 2**  
Boundary conditions of Eq. (25).

x	concentration
gas inlet	0
liquid inlet	$H_{bed}$
gas outlet	$H_{bed}$
liquid outlet	0

For the concentration distribution, the Dirichlet and Danckwerts boundaries were used, and at the exit position, the Neumann boundary was used to define the zero flux, as shown in Table 2, where  $D_{L,i}$  is convection coefficient in the liquid phase, and  $H_{bed}$  (m) is the bed height, which can be obtained from the total bed volume  $V_{bed}$  (m<sup>3</sup>) and the reactor's internal cross-sectional area  $S_R$  (m<sup>2</sup>):

$$H_{bed} = \frac{V_{bed}}{S_R} = \frac{m_p}{S_R \rho_p \varepsilon_S} \quad (31)$$

### 3.3. Calculation of energy consumption

This work numerically analyses the energy consumption associated with reactor operation, focusing on the energy required to maintain gas and liquid flow as well as particle fluidisation within the reactor. Furthermore, a comparable energy loss occurs during rock processing (Xing et al., 2022). The total pressure drop in the reactor is typically considered as the greater of the hydrostatic and frictional pressure drops. Detailed equations can be found in the SI.

### 3.4. Energy consumption for gas and liquid cycle

The cycling of gas phase components typically necessitates the input of compression work, denoted as  $W_G$  (J), to achieve this process:

$$W_G = \frac{1}{\eta} \int_0^t p_{in} Q_a^{in} \frac{\gamma}{\gamma - 1} \left[ \left( \frac{p_{out}}{p_{in}} \right)^{\left( 1 - \frac{1}{\gamma} \right)} - 1 \right] dt \quad (32)$$

where  $\eta$  (-) is the efficiency of the device that outputs the compression work, assumed to be 0.8 in this study.  $\gamma$  (-) is the ratio of specific heat capacity at constant pressure and volume, while  $Q_a^{in}$  (m<sup>3</sup> s<sup>-1</sup>) is the gas flow rate at the inlet,  $p_{in}$  (Pa) and  $p_{out}$  (Pa) refer to the air pressure at the inlet and outlet, respectively.

The water in the reactor is cycled from the bottom to the top, consuming an amount of energy denoted as  $W_L$  (J):

$$W_L = \frac{1}{\eta} \int_0^t \rho_L Q_L g H_{bed} dt \quad (33)$$

where  $Q_L$  (m<sup>3</sup> s<sup>-1</sup>) is the volume flow rate of the liquid.

The total energy consumption of the phase cycle is thus:

$$W_E = W_G + W_L \quad (34)$$

### 3.5. Energy consumption for crushing and mixing

The energy consumption,  $P$  (kW), required for stirring to achieve the desired flow state can be expressed as follows:

$$P = \left( \frac{N_p (7.48 \rho_L / 1330) N^3 (D / 0.3048)^5}{\eta_A 737.56} \right) \quad (35)$$

where  $N_p$  (-), set at 0.35, is the energy parameter, primarily depends on the ratio of impeller blade width ( $W$ ) to impeller diameter ( $D$ ).  $N$  (rps) is the agitator speed,  $D$  (m) is the equivalent diameter of the agitator impeller, and  $\eta_A$ , taken as 0.8, indicates the motor load.

For stirred systems, there exists a critical stirrer speed that ensures complete suspension of particles (Fig. S10). This is defined as the impeller speed at which no particles remain stationary at the reactor bottom for more than 2 s (Zwietering, 1958).

$$N = Sv_L^{0.1} d_p^{0.2} (g(\rho_p - \rho_L)/\rho_L)^{0.45} X^{0.13} (D)^{-0.85} \quad (36)$$

where  $S$  (-) is a parameter of the Zwietering equation, here taken as 5.41 (Ayrancı and Kresta, 2014),  $v_L$  ( $\text{m}^2 \text{s}^{-1}$ ) denotes the kinematic viscosity of the liquid, which is  $8.917 \times 10^{-7} \text{ m}^2 \text{s}^{-1}$ , and  $X$  (%) refers to the volume fraction of the bed occupied by the solid phase.

Energy required to pulverise particles of an initial size  $P_C$  ( $\text{kWh/t}$ ) is calculated using the following equation:

$$P_C = 0.01 W_i \left( \frac{1}{\sqrt{d_{p0}}} - \frac{1}{\sqrt{d_p}} \right) \quad (37)$$

where  $d_{p0}$  (m) is the initial diameter of the particles, and  $W_i$  is the Bond work index, which is  $12.84 \text{ kWh t}^{-1}$  for dolomite.

### 3.6. Energy consumption for $\text{CO}_2$ enrichment

$\text{CO}_2$  enrichment is considered in this work. The total electrical energy required to prepare the feed gas for  $\text{CO}_2$  capture,  $W_{\text{enrich}}$  (J), as follows:

$$W_{\text{enrich}} = \int_0^t RT \left[ \ln \left( \frac{x_{\text{CO}_2}^{\text{air}}}{x_{\text{CO}_2}^{\text{inlet}}} \right) n_{\text{CO}_2}^{\text{top-up}} + \ln \left( \frac{x_{\text{inert}}^{\text{inlet}}}{x_{\text{inert}}^{\text{air}}} \right) n_{\text{inert}}^{\text{top-up}} \right. \\ \left. + \ln \left( \frac{1}{x_{\text{inert}}^{\text{air}}} \right) n_{\text{inert}}^{\text{reject}} \right] dt \quad (38)$$

where  $x_{\text{CO}_2}^{\text{air}}$  (-) is the molar fraction (420 ppm) of  $\text{CO}_2$  in the capture source and inlet.  $x_{\text{inert}}^{\text{air}}$  (-) and  $x_{\text{inert}}^{\text{inlet}}$  (-) represent the molar fractions of noble gases in the capture source.  $n_{\text{CO}_2}^{\text{top-up}}$  ( $\text{mol s}^{-1}$ ) and  $n_{\text{inert}}^{\text{top-up}}$  ( $\text{mol s}^{-1}$ ) are the molar flow rates of  $\text{CO}_2$  and inert gas, respectively, while  $n_{\text{inert}}^{\text{reject}}$  ( $\text{mol s}^{-1}$ ) is the molar flow rate of noble gas produced by the process of producing enriched  $\text{CO}_2$ . This work assumes that  $\text{CO}_2$  enrichment is conducted only once prior to the commencement of each process.

The total electrical energy  $E_{\text{enrich}}$  ( $\text{J kg}^{-1}$ ) required to prepare 1 kg of feed gas for  $\text{CO}_2$  capture is:

$$E_{\text{enrich}} = \xi W_{\text{enrich}} \quad (39)$$

where the conversion rate  $\xi = 14/2.5$  (Xing et al., 2022).

### 3.7. Heat generation and temperature variation

In the EW process, minerals dissolution generates heat, potentially affecting the overall reaction environment. The heat released during the general dolomite reaction, denoted as  $Q$  (kJ), is:

$$Q = -n\Delta H \quad (40)$$

where  $n$  (mol) is the amount of dolomite consumed, and  $\Delta H$  ( $\text{kJ mol}^{-1}$ ) is the enthalpy of dissolution of dolomite. The temperature variations within the system are outlined as follows:

$$\Delta T = \frac{Q}{C_p^c m_c} \quad (41)$$

where  $C_p^c$  ( $\text{kJ kg}^{-1} \text{ K}^{-1}$ ) is the specific heat capacity of the solid-liquid mixture, and  $m_c$  (kg) is the total mass of the mixture. In the slurry system, the aqueous phase and the solid particles can be considered as a combined mixture. The specific heat capacity of this mixture can be determined using the following equation:

$$C_p^c = \sum_i x_i C_p^i \quad (42)$$

where  $C_p^i$  ( $\text{kJ kg}^{-1} \text{ K}^{-1}$ ) is the specific heat capacity of component  $i$ , and:

$$C_p^i = \frac{C_m^i}{M_i} \quad (43)$$

where  $M_i$  ( $\text{kg mol}^{-1}$ ) is the molar mass, and  $C_m^i$  ( $\text{kJ mol}^{-1} \text{ K}^{-1}$ ) is the molar heat capacity (Table 3). According to shomate's formula the molar heat capacity of water can be calculated using the following equation:

$$C_m^W = A + B \frac{T}{1000} + c \left( \frac{T}{1000} \right)^2 + D \left( \frac{T}{1000} \right)^3 + E \left( \frac{T}{1000} \right)^{-2} \quad (44)$$

where A, B, C, D, and E are empirical parameters.

The heat capacity of dolomite  $C_p^D$  ( $\text{kJ mol}^{-1} \text{ K}^{-1}$ ) is expressed as follow (Bénézeth et al., 2018):

$$C_p^D = 547.88 - 0.16759T + 2.840 \times 10^6 T^{-2} - 6547.9T^{-0.5} + 7.7076 \times 10^{-5} T^2 \quad (45)$$

**Table 3**  
Thermodynamic parameter.

Parameter	Unit	Value	Reference
Specific heat capacity of water, $C_p^W$	$\text{kJ kg}^{-1} \text{ K}^{-1}$	4.187	(Xing et al., 2014)
Specific heat capacity of dolomite, $C_p^D$	$\text{kJ kg}^{-1} \text{ K}^{-1}$	0.158	(Bénézeth et al., 2018)
Enthalpy of dolomite, $\Delta H$	$\text{kJ mol}^{-1}$	-2326.73	(Chen et al., 2023)
Specific heat capacity of mixture, $C_p^m$	$\text{kJ kg}^{-1} \text{ K}^{-1}$	1.637–3.780	Calculated

## 4. Results and discussions

### 4.1. Model validation

To evaluate the accuracy of the developed mechanistic model in predicting  $\text{CO}_2$  capture, we measured the mole concentration of  $\text{CO}_2$  in the headspace of the reaction chamber over time with 4 different parameter conditions: liquid-to-gas volume ratio ( $L/G$ ), gas flow rate ( $Q_G$ ), initial  $\text{CO}_2$  concentration ( $x_{\text{CO}_2}$ ) and temperature ( $T$ ). The comparison of experimental and modelling results is shown in Fig. 3. As the reaction progresses,  $\text{CO}_2$  concentration decreases and eventually reaches equilibrium, indicating that the reaction is nearing completion. The results reveal that while deviations in  $\text{CO}_2$  capture rates are observed in some cases (Fig. 3c and 3d), likely due to inadequate sealing under elevated conditions with high  $\text{CO}_2$  concentration and temperature, most predicted results align closely with the experimental data. Notably, errors are smaller under lower  $x_{\text{CO}_2}$ , e.g., 30% and 15%, further suggesting that larger errors are likely caused by gas leakage. Overall, the models are deemed satisfactory in predicting and analysing the effects of various parameters on the  $\text{CO}_2$  capture rate within their studied ranges, as shown in Table 4.

### 4.2. Parameter study of scaled-up reactor

Based on the laboratory-scale rigs utilised for model validation, a parameter study of the scaled-up scenario was conducted to evaluate the batch reactor's performance across the parameter settings listed in Table 4. Five main parameters, including particle diameter ( $d_p$ ), particle loading ( $m_p$ ) (Table S3),  $L/G$ ,  $Q_G$  and  $x_{\text{CO}_2}$ . The parameters were divided into 20 cases (Table S4-S18). For the first 16 cases, the initial  $\text{CO}_2$  concentration was set to 15% to model the flue gas in practical industrial conditions. The particle-related parameters ( $d_p$  and  $m_p$ ) were treated as a distinct category, separate from other cases. Additionally, the concentration of  $\text{CO}_2$  was considered as an "extra category of cases" to assess the reaction under various  $\text{CO}_2$  concentration conditions. Two key metrics,  $\text{CO}_2$  capture rate (CCR) and specific energy consumption (SEC) - were used to evaluate the effects of the five predefined parameters (Chang et al., 2024). CCR is defined as the average hourly  $\text{CO}_2$  capture (kg), while SEC denotes the energy required to capture 1 kg of  $\text{CO}_2$ , over a 120-minutes operation.

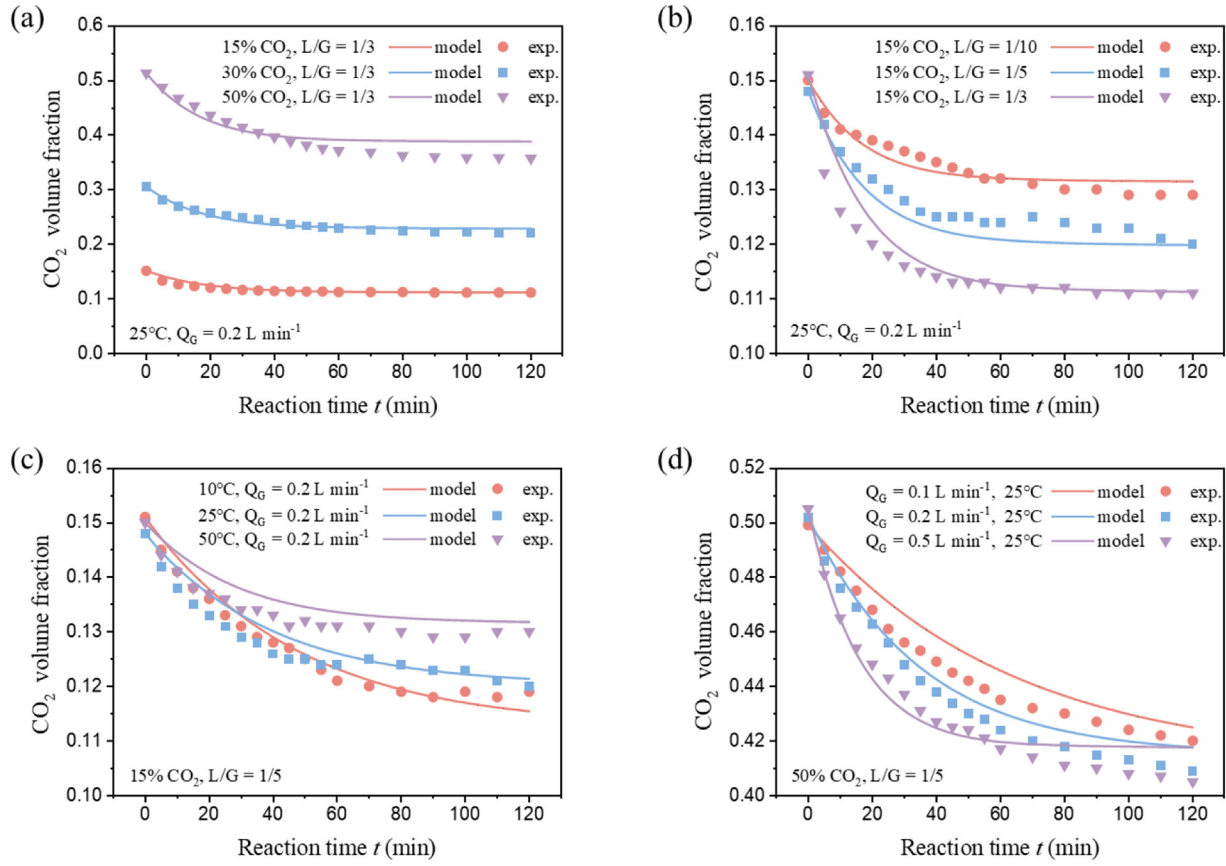


Fig. 3. Results of model validation. Subfigures (a), (b), (c) and (d) are for  $x_{CO_2}$ ,  $L/G$ ,  $T$  and  $Q_G$ .

**Table 4**  
Parametric settings for simulated assessment.

Common parameter	Value	
Operating temperature, $T$	25 °C	
Operating pressure, $P$	1 atm	
Operating time, $t$	120 min	
Radiator volume, $V$	9 m <sup>3</sup>	
Reactor diameter, $d_r$	2 m	
Stirring paddle diameter, $D$	0.8 m	
Liquid circulation volume, $Q_L$	0.002 m <sup>3</sup> s <sup>-1</sup>	
Initial CO <sub>2</sub> concentration, $x_{CO_2}$	Lower limit	Upper limit
Liquid-to-gas volume ratio, $L/G$	1/10	1/1
Particle diameter, $d_p$	0.4 mm	1.0 mm
Particle mass, $m_p$	500 kg	2000 kg
Gas recirculation volume, $Q_G$	0.01 m <sup>3</sup> s <sup>-1</sup>	0.1 m <sup>3</sup> s <sup>-1</sup>

#### 4.3. Effect of particle size ( $d_p$ ) and particle mass ( $m_p$ )

The parameter  $d_p$  is closely related to the total solid-liquid interfacial area, and changes in  $d_p$  influence the rate of mineral dissolution in water (Eq. (12)), potentially impacting the EW rate. Although larger particles dissolve more slowly than smaller ones (Rigopoulos et al., 2018), within the range specified in Table 4, the particle diameter has a limited impact on CCR compared to the other four parameters, indicating that the total specific surface area of the solid particles is not a critical factor in this reaction. As shown in Fig. 4b, the effect of  $d_p$  on energy consumption is significant. This is because particle size significantly influences pressure drop, particle crushing, and the minimum fluidisation stirring rate. Smaller particles increase energy consumption associated with gas circulation and comminution, but it reduces energy consumption related

to agitation. Stirring and material cycling account for the majority of the energy demand (Fig. S5-S8). Smaller  $d_p$  increases pressure loss in the gas cycle, rendering gas-phase cycling highly energy intensive and dominating total energy consumption when  $d_p$  is less than 0.5 mm, although this favours the reduction of the energy required for stirring. In addition, smaller  $d_p$  results in higher energy costs for pellet supply (Eq. (37)), but this is not critical for total energy consumption and accounting for no more than 2%.

Increasing particle loading generally leads to an increase in specific energy consumption due to the increased bed height and the gas needs to overcome a greater pressure drop to pass through the bed (Xing et al., 2021). Concurrently, a higher stirring speed is required during the mixing process due to the increased number of particles (Eq. (36)). This is more pronounced at higher gas flow rate, where energy consumption is more sensitive to changes in particle loading, which is caused by the increased gas flow through the bed per unit time and causes the gas-phase component to consume a larger portion of the total energy consumption (Fig. S6). Generally, particle diameter has a more significant impact on energy consumption than particle loading. Capture performance demonstrates a clear increasing trend with an increase in  $m_p$  for smaller liquid-to-gas volume ratios. Lower  $L/G$  ratios enable more particles to react efficiently with sufficient CO<sub>2</sub>, resulting in a higher CO<sub>2</sub> capture rate. However, as the percentage of liquid increases, the effect of  $m_p$  diminishes, and the gas-liquid mass transfer begins to exhibit greater rate-controlling characteristics. At the highest gas flow rate and lowest liquid-to-gas volume ratio values, the reaction performed the poorest trapping performance and energy consumption across the range of  $m_p$ . This occurs because maintaining a high gas flow rate for gas recirculation demands more energy, while a low liquid-to-gas volume ratio does not provide enough liquid to fully disperse the particles. This inefficiency limits the CO<sub>2</sub> capture rate as the material is not fully utilised.

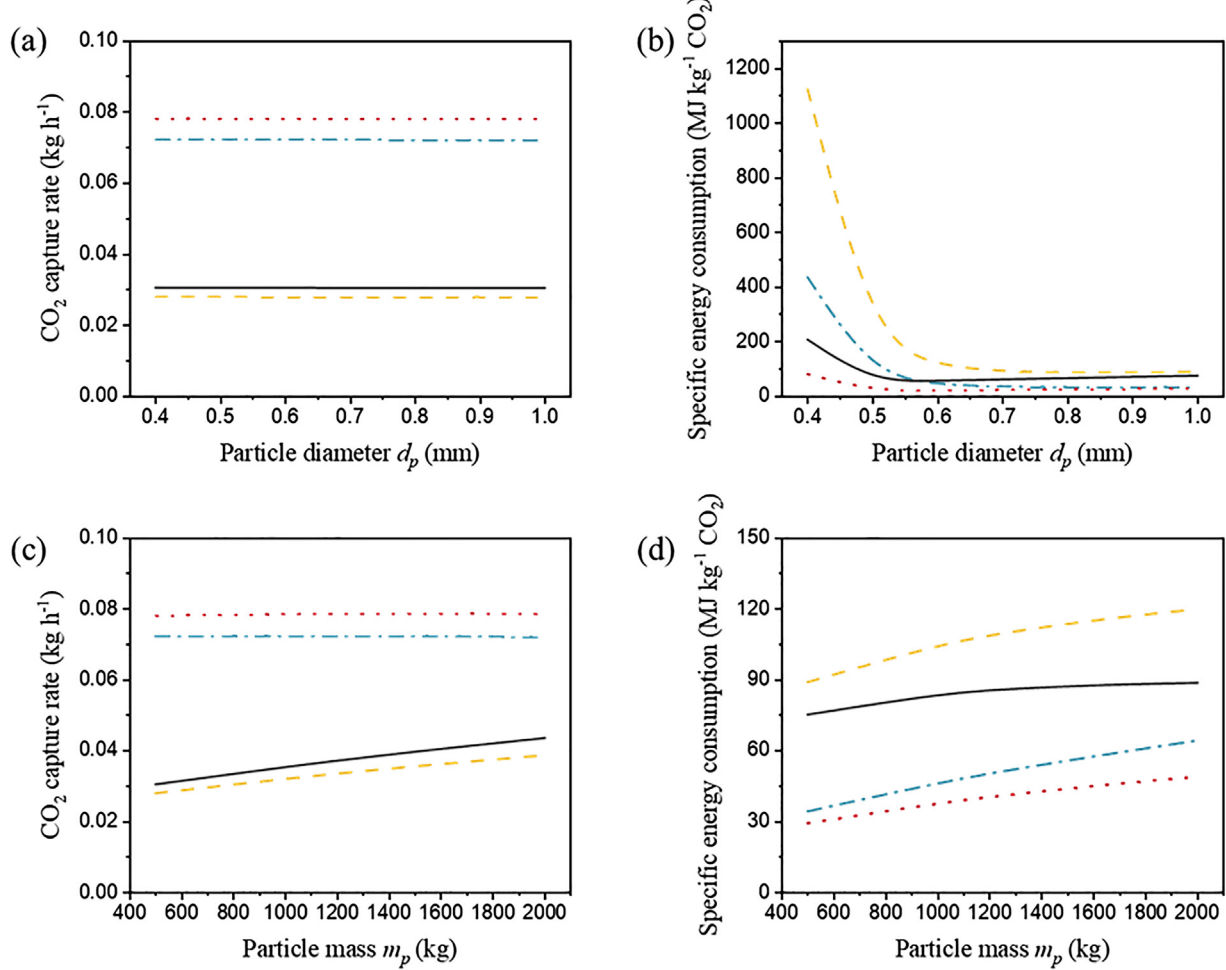


**Fig. 4.** Effect of  $d_p$  (a, b) and  $m_p$  (c, d) on CCR (a, c) and SEC (b, d) at different  $L/G$  and  $Q_G$ . dash dot line –  $L/G = 1, Q_G = 0.1 \text{ m}^3 \text{ s}^{-1}$ ; dash line –  $L/G = 0.1, Q_G = 0.1 \text{ m}^3 \text{ s}^{-1}$ ; dot line –  $L/G = 1, Q_G = 0.01 \text{ m}^3 \text{ s}^{-1}$ ; solid line –  $L/G = 0.1, Q_G = 0.01 \text{ m}^3 \text{ s}^{-1}$ .

#### 4.4. Effect of liquid-to-gas volume ratio ( $L/G$ ) and gas circulation flow rate ( $Q_G$ )

Compared to other parameters, the effect of  $L/G$  significantly impacts both CO<sub>2</sub> capture rate and specific energy consumption, as it is linked to the bed height and the total amount of gas in the headspace of reactor. For CO<sub>2</sub> capture rate, an increase in  $L/G$  leads to enhanced CO<sub>2</sub> capture. This improvement can be attributed to the more effective mixing provided by a higher volume of liquid, which extends the residence time of the bubbles in the solid-liquid mixture and increases the involvement of particle surfaces in the reaction. However, this effect diminishes with higher liquid content because a larger  $L/G$  reduces the gas volume fraction over a fixed reaction time, the rapid CO<sub>2</sub> consumption fails to maintain a sufficient partial pressure, making CO<sub>2</sub> transport from gas to the mixed phase the main rate-limiting step. Regarding specific energy consumption, an increase in  $L/G$  reduces the cost for CO<sub>2</sub> capture, allowing more CO<sub>2</sub> to be captured at the same energy requirement.

Notably, the intersection between the solid line and dot line in Fig. 5c indicates an interaction among particle loading, diameter and liquid-gas ratio, regarding energy consumption. At lower  $L/G$  values (before the intersection), the CO<sub>2</sub> capture rate in case 11 is significantly higher than in case 12. Thus, although energy consumption is greater, the energy consumption in case 12 is higher than in case 11 (Table S4). However, as  $L/G$  continues to increase, the difference in CO<sub>2</sub> capture rate between the cases diminishes, and the energy consumed by the process becomes the key factor affecting the ratio. With a smaller  $m_p$  and larger  $d_p$ , case

12 can achieve a similar CO<sub>2</sub> capture rate as case 11 with lower energy consumption.

As shown in Fig. 5d, the effect of particle loading and diameter on energy consumption grows with increasing gas flow rate for circulation. Although reducing particle size and increasing particle number can enhance CO<sub>2</sub> capture, this benefit is counterbalanced by the additional energy required. Additionally, an increase in  $Q_G$  negates the benefits of smaller  $d_p$ , which typically offer lower stirring energy and slightly higher CCR. Instead, larger particle sizes, which have lower energy consumption of gas pumping, become more advantageous.

Contrary to previous studies, Fig. 5c shows that increasing gas flow rate adversely affects CO<sub>2</sub> capture rate. This suggests the need for further investigation within a more detailed range of  $Q_G$  values. We expanded the range of  $Q_G$  and examined smaller values along with varying initial CO<sub>2</sub> concentration to ensure that these results were not incidental (Fig. S11-S14). Fig. 6 schematically shows that CO<sub>2</sub> capture rate and specific energy consumption do not vary monotonically with  $Q_G$  within its smaller ranges. The primary reason for this behavior is that the weathering rate is influenced by gas-liquid mass transfer.  $Q_G$  affects the superficial gas velocity (Eq. (17)), which in turn influences bubble size (Eq. (21)), bubble rise rate (Eq. (28)), and the mass transfer parameters, including the dispersion coefficient (Eq. (26)) and the mass transfer coefficient for the liquid and gas phases (Eqs. (18) and (19)). When  $Q_G$  exceeds the "inflection point," the rapid gas flow through the bed reduces the contact time between bubbles and the solid-liquid phase, impairing gas-liquid mass transfer due to shortened transfer times.

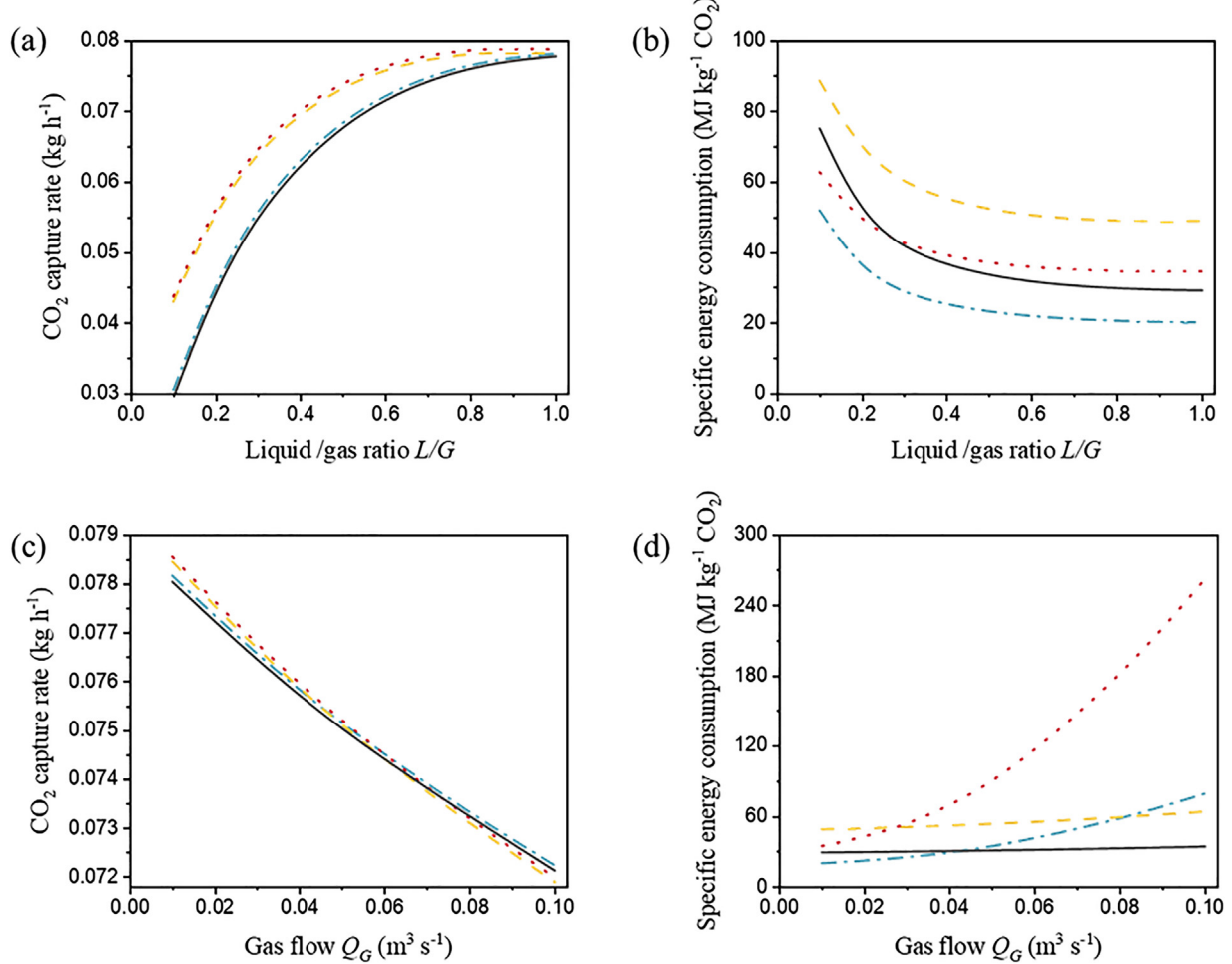


**Fig. 5.** Effect of  $L/G$  (a, b) and  $Q_G$  (c, d) on CCR (a, c) and SEC (b, d) at different  $d_p$  and  $m_p$ . dash dot line –  $d_p = 0.5$  mm,  $m_p = 500$  kg; dash line –  $d_p = 1$  mm,  $m_p = 2000$  kg; dot line –  $d_p = 0.5$  mm,  $m_p = 2000$  kg; solid line –  $d_p = 1$  mm,  $m_p = 500$  kg.

Conversely, at  $Q_G$  values below the "inflection point," the amount of gas involved in the reaction becomes the primary rate-controlling factor, leading to significant variations in CO<sub>2</sub> capture rate and specific energy consumption, increasing  $Q_G$  in this range enhances the CO<sub>2</sub> capture rate.

#### 4.5. Effect of initial CO<sub>2</sub> concentration ( $x_{CO_2}$ )

The performance of EW is influenced by the initial CO<sub>2</sub> concentration. Specifically, four sub-cases were analysed, emphasising variations in  $L/G$ , which significantly affected the results. It was consistently observed in Fig. 7 that an increase in  $x_{CO_2}$  led to a higher specific energy consumption and a lower CO<sub>2</sub> capture rate, regardless of other variables. In terms of energy consumption, a low  $x_{CO_2}$  limits CO<sub>2</sub> removal during the reaction, leading to a higher SEC. Since enrichment constitutes a minor part of overall energy consumption (less than 5%, Fig. S9) and represents 10–50% of the continuous PBC (Table S19) (Xing et al., 2022), increasing  $x_{CO_2}$  through gas enrichment can effectively lower the energy consumption, though this benefit diminishes beyond a certain  $x_{CO_2}$  threshold.

#### 4.6. Effect of temperature

The dissolution equilibrium of the dolomite-water system is influenced by temperature (Robertson et al., 2022), as shown in Eqs. (6)–(8). This process involves several temperature-dependent steps, with the

relevant functions outlined in Table 1. An increase in temperature negatively impacts CO<sub>2</sub> capture efficiency (Fig. 3) by making CO<sub>2</sub> more difficult to dissolve as a dissolved phase in water (Bang et al., 2019), resulting in a lower concentration of bicarbonate ions (the reaction's end product) at equilibrium and increased water consumption. Additionally, elevated temperatures alter various properties of the bed, such as the viscosity coefficient of the liquid phase, significantly affecting the gas-liquid mass transfer time. However, within a specific temperature range, increasing  $T$  can accelerate the slow dissolution rate of minerals (Foteinis et al., 2023). At moderate temperatures, the reactivity of ions increases with temperature due to enhanced ion dissociation (Soong et al., 2006). Concurrently, calcium and magnesium ions are transferred more rapidly to the aqueous phase due to a slight improvement in the transfer mechanism (Nejati and Aghel, 2023). As illustrated in Fig. 3c, higher temperatures reduce the time required for the dissolution rate of the mineral to reach a plateau, though this results in decreased CO<sub>2</sub> capture efficiency.

The release of heat during dolomite particle dissolution is the primary factor causing temperature changes in all cases. According to Eq. (41), the temperature increase in the liquid phase during dolomite dissolution does not exceed 1°C (Table S20), even under the conditions of maximum solubility and minimum heat capacity. Consequently, the impact of mineral dissolution on the reaction system's temperature is negligible in this study. Nevertheless, optimising the capture rate or increasing the capture volume by adjusting temperature remains a viable strategy.

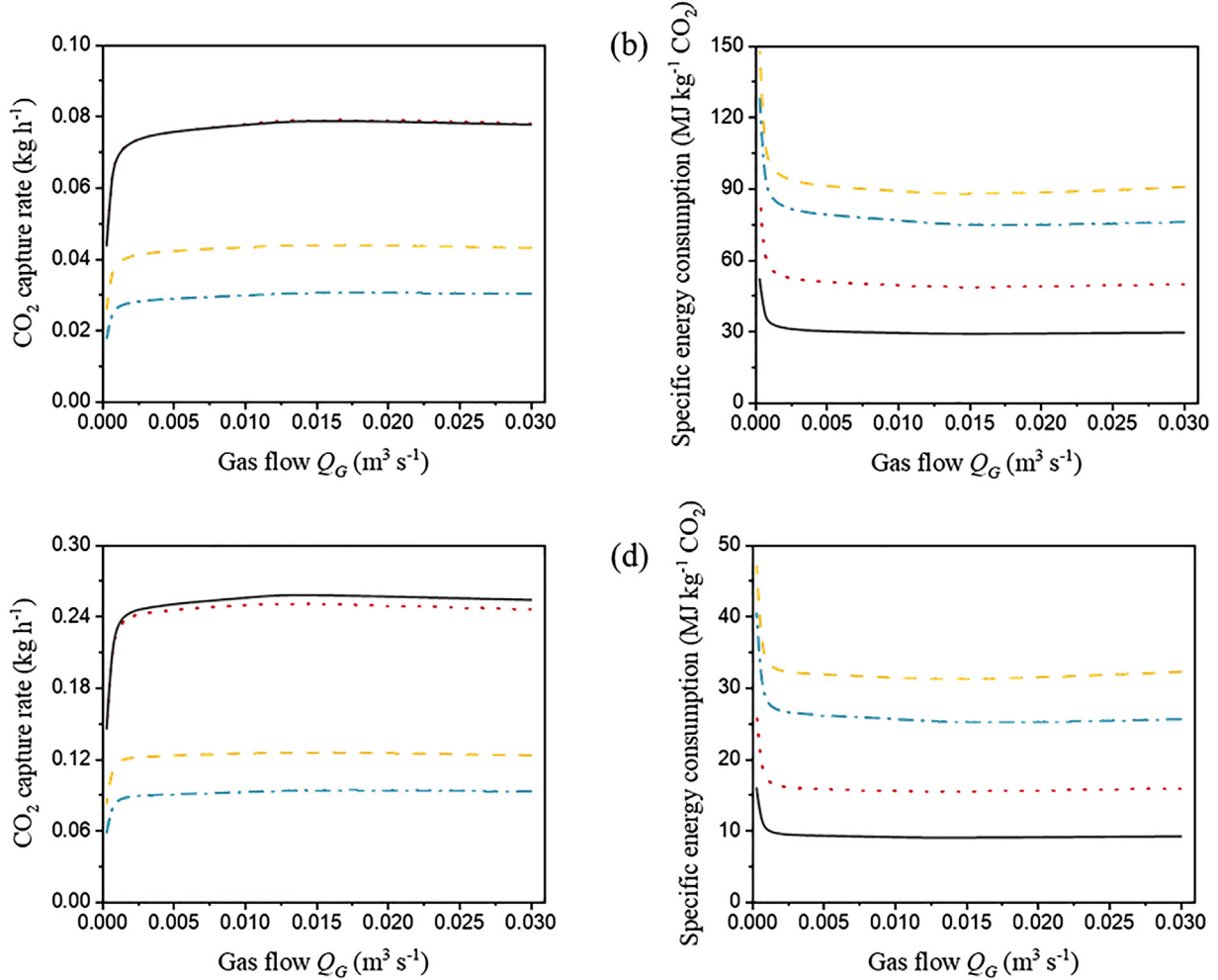


**Fig. 6.** Effect of  $Q_G$  in a smaller range of values on CCR (a, c) and SEC (b, d) at different  $L/G$ ,  $m_p$  and  $x_{CO_2}$  (a and b for  $x_{CO_2} = 0.15$ , c and d for  $x_{CO_2} = 0.5$ ). dash dot line –  $L/G = 0.1$ ,  $m_p = 500$  kg; dash line –  $L/G = 0.1$ ,  $m_p = 2000$  kg; dot line –  $L/G = 1$ ,  $m_p = 2000$  kg; solid line –  $L/G = 1$ ,  $m_p = 500$  kg.

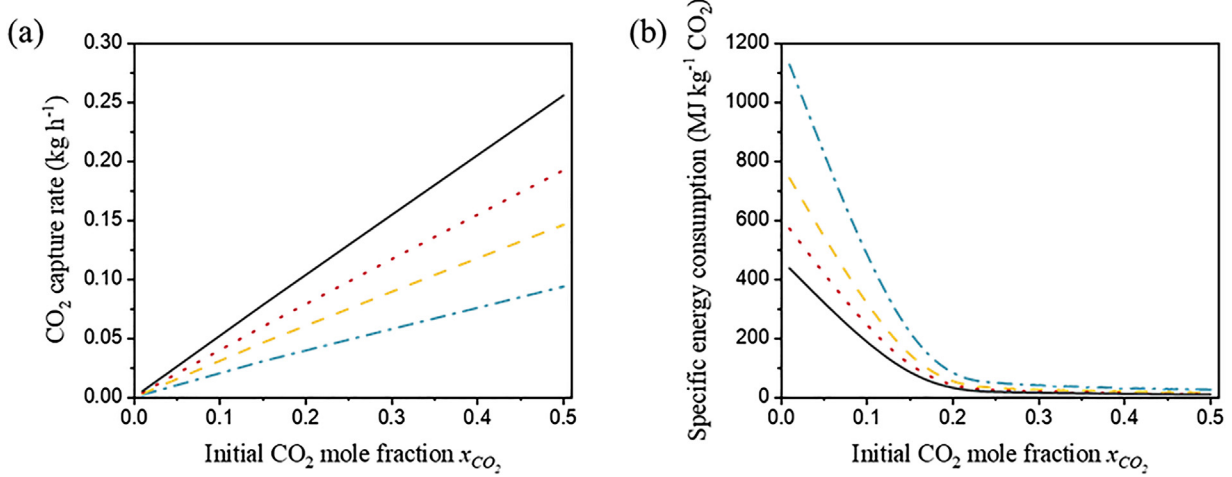


**Fig. 7.** Effect of  $x_{CO_2}$  on CCR (a) and SEC (b) at different  $L/G$ . dash dot line –  $L/G = 0.1$ ; dash line –  $L/G = 0.2$ ; dot line –  $L/G = 1/3$ ; solid line –  $L/G = 1$ .

**Table 5**  
Attainable performance under RSM optimisation results.

Parameter	Design with minimum specific energy consumption	Design with minimum water consumption	Design with maximum CO <sub>2</sub> capture rate	Design with optimal trade-off
$d_p$ (m)	0.0007904	0.0004348	0.0005728	0.0007852
$m_p$ (kg)	1103.75	500	1387.25	1933.25
$L/G$ (-)	0.46855	0.1	0.69265	0.127
$Q_G$ (m <sup>3</sup> s <sup>-1</sup> )	0.01301	0.017695	0.01369	0.01
$x_{CO_2}$ (%)	50%	50%	50%	50%
Specific energy consumption (MJ kg <sup>-1</sup> CO <sub>2</sub> )	8.924	15.576	20.793	11.073
Water consumption (m <sup>3</sup> )	2.888	0.824	3.705	1.289
CO <sub>2</sub> capture rate (kg h <sup>-1</sup> )	0.165	0.122	0.241	0.146

## 5. Multi-variable optimisation and comparison of techniques

### 5.1. Trade-off analysis among multiple indicators

Response surface methodology (RSM) is capable of generating a surrogate model that precisely expresses the relationship between inputs and outputs through functions of independent input variables (Wang et al., 2024). The core of this method involves simultaneously dispersing significant parameters through a set of designed experiments and synthesising the results using a mathematical model to optimise, predict, or interpret the system gradually. To enhance predictions in this multivariable system, RSM was implemented using Design Expert 10 software, incorporating five independent variables and three dependent objectives, i.e., CO<sub>2</sub> capture rate (CCR), specific energy consumption (SEC) and water consumption (WC). A Box-Behnken Design with 46 sampling points was employed, and insignificant terms were excluded to enhance prediction accuracy. The optimisation strategy aimed to identify the optimal design variables within the ranges specified in Table 4, targeting the highest CCR and the lowest SEC and WC. The predicted optimal values of the design variables were validated using results from a physics-based model. The polynomial expressions derived from analyzing these responses are detailed in Section S5 of the SI. Additionally, the predicted R-squared ( $R^2$ ) and Root Mean Square Error (RMSE) values were verified to assess the accuracy of the model.

The  $R^2$  values for water consumption and CO<sub>2</sub> capture rate are 0.9999 and 0.9903, respectively (Fig. 8c and 8d). Their results exhibit high consistency, with most water consumption residuals within  $\pm 0.02$  m<sup>3</sup> and CO<sub>2</sub> capture rate residuals within  $\pm 0.04$  kg h<sup>-1</sup>. The  $R^2$  for specific energy consumption is relatively low, particularly for high specific energy consumption where deviations are significant. After excluding outliers, specific energy consumption residuals range within  $\pm 25$  MJ kg<sup>-1</sup> CO<sub>2</sub>. Accuracy improves with the inclusion of lower data points. Since high specific energy consumption is only relevant under extreme conditions and is not prioritized in most scenarios, the model can be considered to have high prediction accuracy for the three dependent variables.

Fig. 8a visualizes the predicted objectives, energy and water consumption, and CO<sub>2</sub> capture rate from the simulation results. The simulation dataset includes 216 points from previously studied scenarios, which also includes the four predictive values suggested by RSM.

Table 5 presents the predicted results for various objectives. Achieving optimal specific energy consumption requires balancing different parameters. Minimising SEC requires balancing  $L/G$  and  $m_p$ , while  $d_p$  should also be considered. A higher  $m_p$  necessitates a lower  $L/G$  to ensure adequate CO<sub>2</sub> participation in the reaction, whereas a higher  $L/G$  is necessary to provide sufficient water for mineral dissolution. Efficient gas circulation also enhances energy efficiency. When these factors are combined, the resulting energy consumption is 8.924 MJ kg<sup>-1</sup> CO<sub>2</sub>.

Although the model operates with a fixed volume of water, restricting the range of water consumption as shown in Fig. 8c, two parameters (i.e.,  $L/G$  and  $m_p$ ) demonstrate a distinct correlation with water consumption. The simulation indicates that optimal water utilization is achieved with the lowest liquid and gas ratio and the highest gas volume, which can be attributed to minimising the mass of particles and the volume of water inside the reactor. This is because an excess of minerals relative to gas suggests that increasing the gas volume improves water utilisation, thereby resulting in minimal water consumption of 0.824 m<sup>3</sup>. Other parameters show little correlation with water consumption once maximum utilisation is achieved (Fig. 9).

For maximum CO<sub>2</sub> capture rate, the recommended values for  $Q_G$  are consistent with the conclusions in the previous section, and the maximum  $x_{CO_2}$  also aligns with the objectives. In this scenario, achieving the removal rate of 0.241 kg h<sup>-1</sup> requires significantly higher energy consumption.

Table 5 presents the trade-off solution derived from the RSM model, where the three objectives are optimally balanced. The maximum CO<sub>2</sub> concentration remains advantageous due to the lower energy consumption required for gas enrichment. However, it is important to note that this model simplifies reality by not accounting for additional energy demands, such as mineral transport. The calculations also carry inherent uncertainties due to the complex and variable nature of the system. Therefore, validation under real-world conditions would be beneficial to confirm the model's applicability.

### 5.2. Comparison of capture rate and energy consumption across other systems

Given that continuous systems can sustain the highest reaction rates, the performance of the SSR during the first 10 min, based on the RSM results, is compared with the optimised TBC and PBC models using the surrogate model. The SSR significantly reduces water consumption, which is 0.9045 m<sup>3</sup>, corresponding to 60% of the TBC (1.4928 m<sup>3</sup>) and PBC (1.4966 m<sup>3</sup>). This enables a CO<sub>2</sub> capture rate of 1.11 kg h<sup>-1</sup> in the SSR, comparable to 0.73 kg h<sup>-1</sup> in the TBC and 1.91 kg h<sup>-1</sup> in the PBC, suggesting a potentially higher initial capture rate in the SSR compared to the other reactors. Targeting CO<sub>2</sub> capture efficiency, the SSR demonstrated an efficiency of 2.93 kg h<sup>-1</sup>, surpassing the 2.01 kg h<sup>-1</sup> in the PBC system. Additionally, the SSR's specific energy consumption (1.2567 MJ kg<sup>-1</sup> CO<sub>2</sub>) and water consumption (3.6675 m<sup>3</sup> kg<sup>-1</sup> CO<sub>2</sub>) are lower than those of the PBC (1.7331 MJ kg<sup>-1</sup> CO<sub>2</sub> and 14.142 m<sup>3</sup> kg<sup>-1</sup> CO<sub>2</sub>, respectively), although its performance is slightly inferior to that of the TBC in this context. The relatively higher energy consumption of the SSR for CO<sub>2</sub> capture can be attributed to decreasing CO<sub>2</sub> concentrations in the headspace gas and an increase in bicarbonate ions in the water. This leads to diminishing capture performance over time, along with the excessive energy requirements for stirring, adversely affects overall efficiency and results in an energy consumption of 0.9853 MJ kg<sup>-1</sup> CO<sub>2</sub>. However, this approach achieves a water consumption of 2.9167 m<sup>3</sup> and

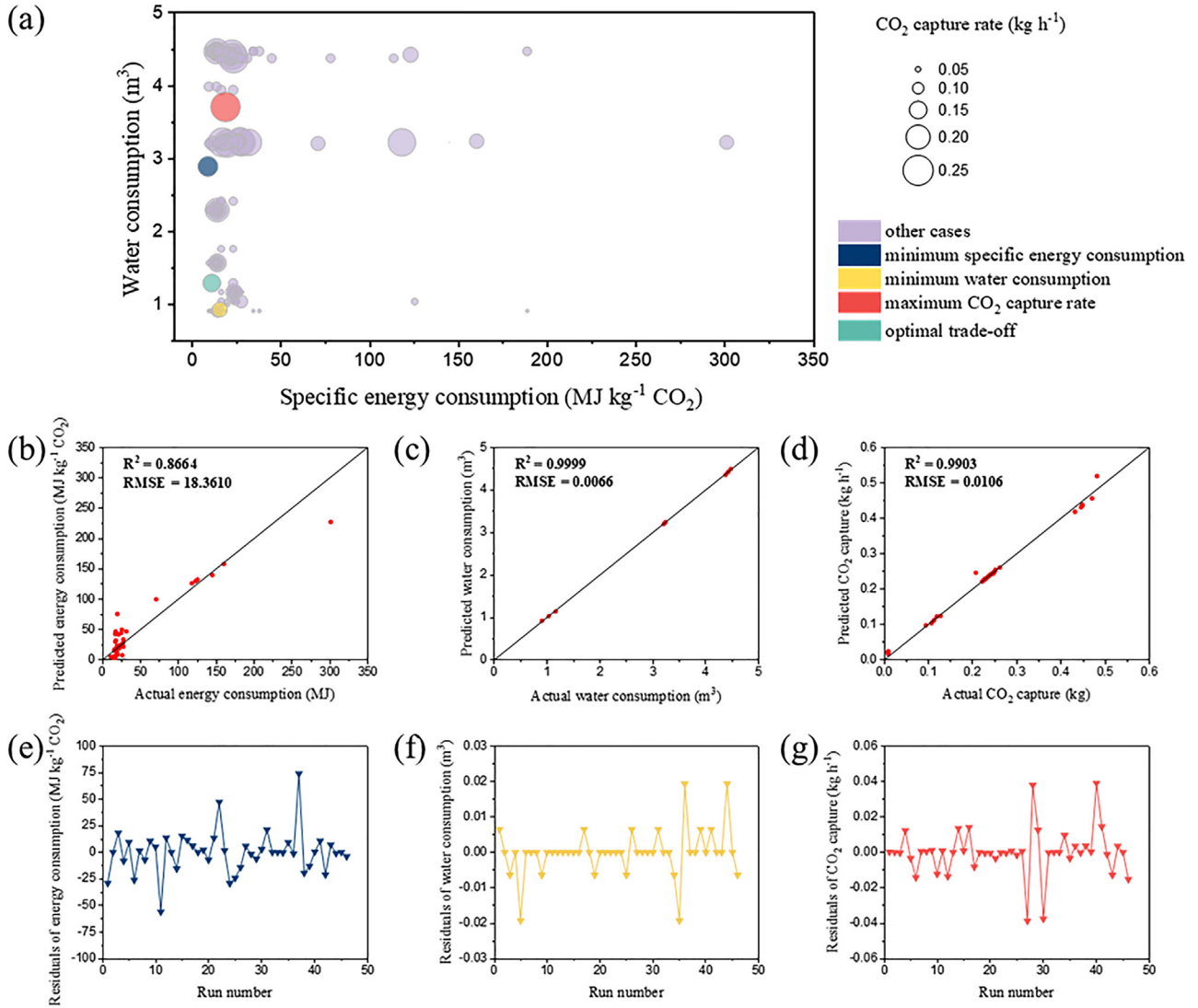


**Fig. 8.** (a) Results of the cases and RSM optimised solutions. (b-g) Accuracy of the surrogate models in terms of RMSE,  $R^2$  and residuals. (b, e): The SEC model; (c, f): The WC model; (d, g): The CCR model.

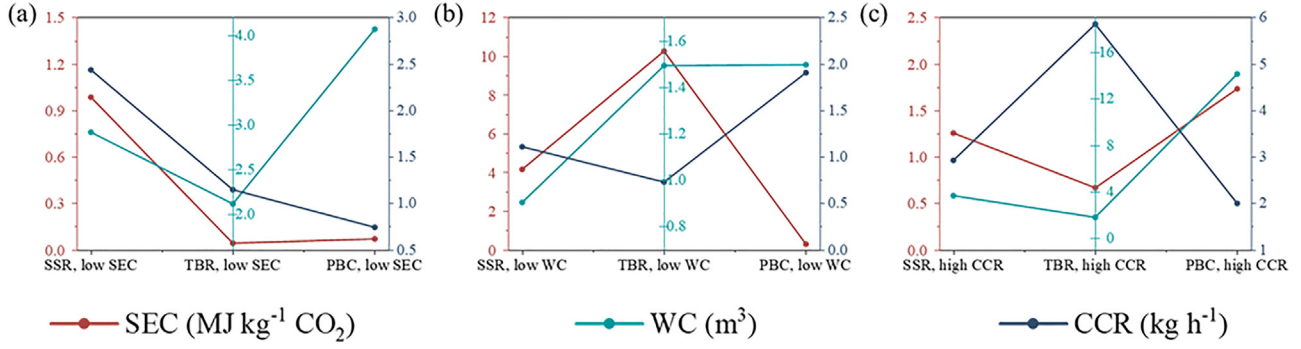


**Fig. 9.** Comparison of optimisation results for SEC, WC and CCR across different systems with minimum specific energy consumption (a), water consumption (b) and maximum  $\text{CO}_2$  capture rate (c) targets.

an impressive capture rate of  $2.44 \text{ kg CO}_2 \text{ h}^{-1}$ , while the potential uplift from the updraft in the system facilitates mixing, which helps reduce operational energy consumption.

The energy consumption of broader direct air capture (DAC) technologies is also a key focus of our attention. The energy demand for alkali-based aqueous processes ranges from  $5.43$  to  $7.9 \text{ MJ kg}^{-1} \text{ CO}_2$

(Keith et al., 2018; Wu et al., 2022). Evaluations of other adsorption processes, such as alkali and MEA scrubbing, indicate that the energy costs per kg of  $\text{CO}_2$  captured are  $6.21 - 6.48 \text{ MJ}$  and  $20.04 - 49.32 \text{ MJ}$ , respectively (Sabatino et al., 2021). As a common process in DAC, Wu et al. (2022) suggested that temperature vacuum swing adsorption requires  $1.93 - 23.09 \text{ MJ}$  of energy to process 1 kg of  $\text{CO}_2$ . Recent

studies have also evaluated DAC using solid and liquid solvents systems, indicating energy requirements of  $0.5 - 18.75 \text{ MJ kg}^{-1} \text{ CO}_2$  and  $0.62 - 17.28 \text{ MJ kg}^{-1} \text{ CO}_2$ , respectively (An et al., 2023). The study of Seo and Hatton (2023) on electrochemical direct air capture reports an energy demand of  $1.48 \text{ MJ kg}^{-1} \text{ CO}_2$ . These technologies demonstrate varying degrees of significant reliance on energy consumption. Some studies on DAC using minerals have also considered potential energy requirements. For instance, the energy consumption of mineral carbonation storage solutions ranges from  $2.5 - 4 \text{ MJ kg}^{-1} \text{ CO}_2$  (Goldberg et al., 2023), while DAC combined with mineral and renewable resource like wind energy achieves efficiencies of approximately  $1.5 - 3.11 \text{ MJ kg}^{-1} \text{ CO}_2$  (Goldberg et al., 2013; Myers and Nakagaki, 2020). Although the performance of these carbon capture technologies may vary significantly under different conditions, leading to uncertainties in energy consumption estimates, the energy demand for implementing EW within reactors remains comparatively low, even when accounting for the degassing of  $\text{CO}_2$  into the atmosphere due to the change of natural environment.

## 6. Conclusion

A batch stirred-slurry reactor (SSR) system is developed for investigating  $\text{CO}_2$  capture through the enhanced weathering of dolomite. Both physics-based mechanistic simulations and data-driven models are employed for multi-variable parametric studies and optimisation.

An inlet  $\text{CO}_2$  concentration of 15% is used in most studied cases to represent the typical flue gas emitted from power plants. Our research discovered the optimal volume fraction and size of solid particles by evaluating the  $\text{CO}_2$  capture rate and the energy required for particle crushing,  $\text{CO}_2$  enrichment, stirring, and gas and liquid circulation, which significantly contribute to the overall energy consumption. It is found that the  $\text{CO}_2$  capture performance of the SSR system is strongly determined by the gas-liquid mass transfer, revealing the significant influence of bubble resident time and gas-liquid interfacial area. This work also highlights the contradictory effect of gas circulation volumetric flow rate on  $\text{CO}_2$  capture performance, where the interplay between bubble size, rising velocity, and mass transfer coefficient creates a complex dynamic. The fast reaction achieved, despite the high energy cost of stirring, may make this work particularly relevant for slower-reacting minerals. Additionally, enhancing the  $\text{CO}_2$  capture rate by varying temperatures, such as utilizing high-temperature flue gases, is worth considering.

The interactions among multiple objectives are further explored, emphasizing that RSM models, where  $R^2$  values for water consumption, and  $\text{CO}_2$  capture rate all exceed 0.99, are reliable for performance predictions at scales. Although the  $R^2$  for energy consumption predictions is approximately 0.87, the predictions are considered accurate for energy consumption below  $25 \text{ MJ kg}^{-1} \text{ CO}_2$ . In the scaled-up scenario, a higher initial  $\text{CO}_2$  concentration benefits all objectives. Achieving the lowest energy consumption requires balancing various parameters; the minimal water consumption is primarily influenced by the volume fraction of mineral and the liquid-to-gas volume ratio, while the main factors affecting the  $\text{CO}_2$  capture rate are the gas circulation rate and the liquid-to-gas volume ratio. The most balanced scenario achieves an energy consumption of  $11.073 \text{ MJ kg}^{-1} \text{ CO}_2$ , a water consumption of  $1.289 \text{ m}^3$ , and a  $\text{CO}_2$  capture rate of  $0.146 \text{ kg h}^{-1}$ .

This study investigates the potential effects of operational setups on an EW-based  $\text{CO}_2$  capture system. The model elucidates the mechanistic effects of various factors on key performance indicators, demonstrating that optimising operating parameters can significantly improve  $\text{CO}_2$  capture rates and reduce energy consumption. The optimised results deliver performance comparable to commercial systems, offering valuable insights for engineering designs targeted at large-scale deployment.

## Declaration of competing interest

The authors declare that they have no known competing financial interests or personal relationships that could have appeared to influence the work reported in this paper.

## CRediT authorship contribution statement

**Yalun Zhao:** Writing – original draft, Validation, Investigation, Data curation. **Mingliang Wang:** Visualization, Formal analysis. **Jin Xuan:** Methodology, Funding acquisition. **Dengao Chang:** Writing – review & editing, Project administration. **Ziming Li:** Investigation. **Shiyu Wang:** Formal analysis. **Yun Ou:** Formal analysis. **Xu Wang:** Writing – review & editing, Supervision, Resources. **Lei Xing:** Writing – review & editing, Supervision, Methodology, Conceptualization.

## Acknowledgements

The authors disclosed receipt of the financial supported by the National Key R&D program of China (2019YFD1101301), the Three Gorges Joint Fund from the Science and Technology Department of Hubei Province (2023AFD193), and the Environmental protection Scientific Research Project of Department of Ecology and Environment of Hubei Province (2023ZHB-06).

## Supplementary materials

Supplementary material associated with this article can be found, in the online version, at doi:10.1016/j.ccst.2025.100363.

## References

- Adhikari, B., Orme, C.J., Stetson, C., Klaehn, J.R., 2023. Techno-economic analysis of carbon dioxide capture from low concentration sources using membranes. *Chem. Eng. J.* 474, 14.
- Akita, K., Yoshida, F., 1973. Gas holdup and volumetric mass transfer coefficient in bubble columns. Effects of liquid properties. *Ind. Eng. Chem. Res.* 12 (1), 76–80.
- An, K.J., Li, K., Yang, C.M., Brecht, J., Nawaz, K., 2023. A comprehensive review on regeneration strategies for direct air capture. *J. CO<sub>2</sub> Util.* 76, 16.
- Ayrancı, I., Kresta, S.M., 2014. Critical analysis of Zwierterring correlation for solids suspension in stirred tanks. *Chem. Eng. Res. Des.* 92 (3), 413–422.
- Bang, J.H., Chae, S.C., Lee, S.W., Kim, J.W., Song, K., Kim, J., Kim, W., 2019. Sequential carbonate mineralization of desalination brine for  $\text{CO}_2$  emission reduction. *J. CO<sub>2</sub> Util.* 33, 427–433.
- Beerling, D.J., Kantzas, E.P., Lomas, M.R., Wade, P., Eufrasio, R.M., et al., 2020. Potential for large-scale  $\text{CO}_2$  removal via enhanced rock weathering with croplands. *Nature* 583, 242–248.
- Bénézeth, P., Berninger, U.N., Bovet, N., Schott, J., Oelkers, E.H., 2018. Experimental determination of the solubility product of dolomite at 50–253 °C. *Geochim. Cosmochim. Acta* 224, 262–275.
- Benyahia, F., O'Neill, K.E., 2005. Enhanced voidage correlations for packed beds of various particle shapes and sizes. *Part. Sci. Technol.* 23 (2), 169–177.
- Bezerra, M.A., Santelli, R.E., Oliveira, E.P., Villar, L.S., Escalera, L.A., 2008. Response surface methodology (RSM) as a tool for optimization in analytical chemistry. *Talanta* 76 (5), 965–977.
- Bin, A.K., 1984. Mass transfer to the free interface in stirred vessels. *Chem. Eng. Commun.* 31 (1–6), 155–183.
- Busenberg, E., Plummer, L.N., 1982. The kinetics of dissolution of dolomite in  $\text{CO}_2\text{-H}_2\text{O}$  systems at 1.5 to 65 °C and 0 to 1 atm  $\text{PCO}_2$ . *Am. J. Sci.* 282, 45–78.
- Cents, A.H.G., Brilman, D.W.F., Versteeg, G.F., 2005.  $\text{CO}_2$  absorption in carbonate/bicarbonate solutions: The Danckwerts-criterion revisited. *Chem. Eng. Sci.* 60 (21), 5830–5835.
- Chang, D.G., Luo, Y., Song, S.Y., Huang, Y., Zhao, Y.L., Ou, Y., Li, Z.M., Wang, X., 2024. Continuous peroxymonosulfate activation by a novel  $\text{CoFe}_2\text{O}_4$ -functionalized carbon fiber electroactive filter towards ultrafast and cost-effective decontamination: performance, mechanism and application. *Chem. Eng. J.* 502, 14.
- Chen, C., Zhong, H.T., Wang, X.Y., Ning, M., Wang, X., Ge, Y.Z., Wang, H., Tang, R.F., Hou, M.C., 2023. Thermodynamic and kinetic studies of dolomite formation: a review. *Minerals* 13 (12), 21.
- Chen, C.L., Lee, J.Y., 2010. On the use of graphical analysis for the design of batch water networks. *Clean Technol. Environ. Policy* 12 (2), 117–123.
- Chou, L., Garrels, R.M., Wollast, R., 1989. Comparative study of the kinetics and mechanisms of dissolution of carbonate minerals. *Chem. Geol.* 78 (3–4), 269–282.
- Danckwerts, P.V., 1995. Continuous flow systems. Distribution of residence times. *Chem. Eng. Sci.* 50 (24), 3857–3866.

- Darton, R.C., 1985. Physical behaviour of three-phase fluidized beds. *Fluidization* 495–528.
- Darton, R.C., Harrison, D., 1985. Some properties of gas bubbles in three-phase fluidized beds. In: *Multi-Phase Flow Systems Symposium* (2nd International Conference on Multi-phase Flow). London, England, pp. B1–28.
- Du, A.D., Lattanzi, L., Jarfors, A.E.W., Zheng, J.C., Wang, K.K., Yu, G.G., 2023. On the efficient particle dispersion and transfer in the fabrication of SiC-particle-reinforced aluminum matrix composite. *Crystals (Basel)* 13 (12), 15.
- Edwards, T.J., Maurer, G., Newman, J., Prausnitz, J.M.J.A.J., 1978. Vapor-liquid equilibria in multicomponent aqueous solutions of volatile weak electrolytes. *AIChE J.* 24, 966–976.
- Feng, D.Y., Hicks, A., 2023. Environmental, human health, and CO<sub>2</sub> payback estimation and comparison of enhanced weathering for carbon capture using wollastonite. *J. Clean. Prod.* 414, 11.
- Foteinis, S., Campbell, J.S., Renforth, P., 2023. Life cycle assessment of coastal enhanced weathering for carbon dioxide removal from air. *Environ. Sci. Technol.* 57 (15), 6169–6178.
- Fuhrman, J., Bergero, C., Weber, M., Monteith, S., Wang, F.M., Clarens, A.F., Doney, S.C., Shobe, W., McJeon, H., 2023. Diverse carbon dioxide removal approaches could reduce impacts on the energy-water-land system. *Nat. Clim. Chang.* 13 (4), 341–+.
- Goldberg, D.S., Lackner, K.S., Han, P., Slagle, A.L., Wang, T., 2013. Co-Location of air capture, subseafloor CO<sub>2</sub> sequestration, and energy production on the Kerguelen plateau. *Environ. Sci. Technol.* 47 (13), 7521–7529.
- Goldberg, D.S., Nawaz, S., Lavin, J., Slagle, A.L., 2023. Upscaling DAC hubs with wind energy and CO<sub>2</sub> mineral storage: considerations for large-scale carbon removal from the atmosphere. *Environ. Sci. Technol.* 57 (51), 21527–21534.
- Goll, D.S., Ciais, P., Amann, T., Buermann, W., Chang, J.F., Eker, S., Hartmann, J., Janssens, I., Li, W., Obersteiner, M., Penelas, J., Tanaka, K., Vicca, S., 2021. Potential CO<sub>2</sub> removal from enhanced weathering by ecosystem responses to powdered rock. *Nat. Geosci.* 14 (8), 545–+.
- Hangx, S.J.T., Spiers, C.J., 2009. Coastal spreading of olivine to control atmospheric CO<sub>2</sub> concentrations: a critical analysis of viability. *Int. J. Greenhouse Gas Control* 3 (6), 757–767.
- Hartmann, J., West, A.J., Renforth, P., Köhler, P., De La Rocha, C.L., Wolf-Gladrow, D.A., Dürr, H.H., Scheffran, J., 2013. Enhanced chemical weathering as a geoengineering strategy to reduce atmospheric carbon dioxide, supply nutrients, and mitigate ocean acidification. *Rev. Geophys.* 51 (2), 113–149.
- Hikita, H., Asai, S., Takatsuka, T.J.C.E.J., 1976. Absorption of carbon dioxide into aqueous sodium hydroxide and sodium carbonate-bicarbonate solutions. *Chem. Eng. J.* 11 (2), 131–141.
- Ilauta, I., Larachi, F., 2012. New scrubber concept for catalytic CO<sub>2</sub> hydration by immobilized carbonic anhydrase II and in-situ inhibitor removal in three-phase monolith slurry reactor. *Sep. Purif. Technol.* 86, 199–214.
- Jiang, H., Wang, S., Xing, L., Pinfield, V.J., Xuan, J., 2023. Machine learning based techno-economic process optimisation for CO<sub>2</sub> capture via enhanced weathering. *Energy AI* 12, 15.
- Kantzas, E.P., Martin, M.V., Lomas, M.R., Eufrasio, R.M., Renforth, P., et al., 2022. Substantial carbon drawdown potential from enhanced rock weathering in the United Kingdom. *Nat. Geosci.* 15, 382–389.
- Keith, D.W., Holmes, G., Angelo, D.S., Heidel, K., 2018. A process for capturing CO<sub>2</sub> from the atmosphere. *Joule* 2 (8), 1573–1594.
- Lefebvre, D., Goglio, P., Williams, A., Manning, D.A.C., de Azevedo, A.C., Bergmann, M., Meersmans, J., Smith, P., 2019. Assessing the potential of soil carbonation and enhanced weathering through Life Cycle Assessment: a case study for São Paulo State, Brazil. *J. Clean. Prod.* 233, 468–481.
- Lekhal, A., Chaudhari, R.V., Wilhelm, A.M., Delmas, H., 1997. Gas-liquid mass transfer in gas-liquid-liquid dispersions. *Chem. Eng. Sci.* 52 (21–22), 4069–4077.
- Moosdorff, N., Renforth, P., Hartmann, J., 2014. Carbon dioxide efficiency of terrestrial enhanced weathering. *Environ. Sci. Technol.* 48 (9), 4809–4816.
- Myers, C., Nakagaki, T., 2020. Direct mineralization of atmospheric CO<sub>2</sub> using natural rocks in Japan. *Environ. Res. Lett.* 15 (12), 12.
- Nejati, K., Aghel, B., 2023. Utilizing fly ash from a power plant company for CO<sub>2</sub> capture in a microchannel. *Energy* 278, 12.
- Oelkers, E.H., Declercq, J., Saldi, G.D., Gislason, S.R., Schott, J., 2018. Olivine dissolution rates: a critical review. *Chem. Geol.* 500, 1–19.
- Pokrovsky, O.S., Schott, J., 2001. Kinetics and mechanism of dolomite dissolution in neutral to alkaline solutions revisited. *Am. J. Sci.* 301 (7), 597–626.
- Powis, C.M., Smith, S.M., Minx, J.C., Gasser, T., 2023. Quantifying global carbon dioxide removal deployment. *Environ. Res. Lett.* 18 (2), 11.
- Prabhakar, S., Bandyopadhyay, S., 2023. Optimum integration of negative emission technologies for carbon-constrained energy sector planning. *J. Clean. Prod.* 411, 12.
- Prado, A., Mac Dowell, N., 2023. The cost of permanent carbon dioxide removal. *Joule* 7 (4), 700–712.
- Rau, G.H., 2011. CO<sub>2</sub> mitigation via capture and chemical conversion in seawater. *Environ. Sci. Technol.* 45 (3), 1088–1092.
- Reershemius, T., Kelland, M.E., Jordan, J.S., Davis, I.R., D'Ascanio, R., Kalderon-Asael, B., Asael, D., Suhrhoff, T.J., Epikhov, D.Z., Beerling, D.J., Reinhard, C.T., Planavsky, N.J., 2023. Initial validation of a soil-based mass-balance approach for empirical monitoring of enhanced rock weathering rates. *Environ. Sci. Technol.* 57 (48), 19497–19507.
- Renforth, P., 2012. The potential of enhanced weathering in the UK. *Int. J. Greenhouse Gas Control* 10, 229–243.
- Renforth, P., 2019. The negative emission potential of alkaline materials. *Nat. Commun.* 10, 8.
- Renforth, P., Henderson, G., 2017. Assessing ocean alkalinity for carbon sequestration. *Rev. Geophys.* 55 (3), 636–674.
- Rigopoulos, I., Harrison, A.L., Delimitis, A., Ioannou, I., Efsthathiou, A.M., Kyrtasi, T., Oelkers, E.H., 2018. Carbon sequestration via enhanced weathering of peridotites and basalts in seawater. *Appl. Geochem.* 91, 197–207.
- Robertson, H.A., Corlett, H., Hollis, C., Whitaker, F.F., 2022. Solubility product constants for natural dolomite (0–200 °C) through a groundwater-based approach using the usgs produced water database. *Am. J. Sci.* 322 (4), 593–645.
- Sabatino, F., Grimm, A., Gallucci, F., Annaland, M.V., Kramer, G.J., Gazzani, M., 2021. A comparative energy and costs assessment and optimization for direct air capture technologies. *Joule* 5 (8), 2047–2076.
- Seo, H., Hatton, T.A., 2023. Electrochemical direct air capture of CO<sub>2</sub> using neutral red as reversible redox-active material. *Nat. Commun.* 14 (1), 11.
- Soong, Y., Fauth, D.L., Howard, B.H., Jones, J.R., Harrison, D.K., Goodman, A.L., Gray, M.L., Frommell, E.A., 2006. CO<sub>2</sub> sequestration with brine solution and fly ashes. *Energy Convers. Manag.* 47 (13–14), 1676–1685.
- Taylor, L.L., Quirk, J., Thorley, R.M.S., Kharecha, P.A., Hansen, J., Ridgwell, A., Lomas, M.R., Banwart, S.A., Beerling, D.J., 2016. Enhanced weathering strategies for stabilizing climate and averting ocean acidification. *Nat. Clim. Chang.* 6 (4), 402–+.
- Terlouw, T., Bauer, C., Rosa, L., Mazzotti, M., 2021. Life cycle assessment of carbon dioxide removal technologies: a critical review. *Energy Environ. Sci.* 14 (4), 1701–1721.
- Tsonopoulos, C., Coulson, D.M., Inman, L.B., 1976. Ionization constants of water pollutants. *J. Chem. Eng. Data* 21 (2), 190–193.
- Wang, S.Y., Li, F., Sadhukhan, J., Xuan, J., Mao, X.H., Xing, L., Zhao, X., Wang, X., 2024. Revealing the best solution simultaneously for environmental and economic performance using response surface methodology under the perspective of life cycle: a case study of sludge dewatering by the Fenton process. *J. Clean. Prod.* 434, 11.
- Witek-Krowiak, A., Chojnacka, K., Podstawczyk, D., Dawiec, A., Bubala, K., 2014. Application of response surface methodology and artificial neural network methods in modelling and optimization of biosorption process. *Bioresour. Technol.* 160, 150–160.
- Wu, X.W., Krishnamoorti, R., Bollini, P., 2022. Technological options for direct air capture: a comparative process engineering review. *Annu. Rev. Chem. Biomol. Engineer.* 13, 279–300.
- Xing, L., Darton, R.C., Yang, A.D., 2021. Enhanced weathering to capture atmospheric carbon dioxide: modeling of a trickle-bed reactor. *AIChE J.* 67 (5), 18.
- Xing, L., Jiang, H., Tian, X.J., Yin, H.J., Shi, W.D., Yu, E.L., Pinfield, V.J., Xuan, J., 2023a. Combining machine learning with multi-physics modelling for multi-objective optimisation and techno-economic analysis of electrochemical CO<sub>2</sub> reduction process. *Carbon Capture Sci. Technol.* 9, 11.
- Xing, L., Jiang, H., Wang, S., Pinfield, V.J., Xuan, J., 2023b. Data-driven surrogate modelling and multi-variable optimization of trickle bed and packed bubble column reactors for CO<sub>2</sub> capture via enhanced weathering. *Chem. Eng. J.* 454, 139997.
- Xing, L., Liu, X.T., Alaje, T., Kumar, R., Mamlouk, M., Scott, K., 2014. A two-phase flow and non-isothermal agglomerate model for a proton exchange membrane (PEM) fuel cell. *Energy* 73, 618–634.
- Xing, L., Pullin, H., Bullock, L., Renforth, P., Darton, R.C., Yang, A.D., 2022. Potential of enhanced weathering of calcite in packed bubble columns with seawater for carbon dioxide removal. *Chem. Eng. J.* 431, 134096.
- Zhang, J.Y., Yang, A.D., Darton, R., Xing, L., Vaughan, A., 2023. Surrogate modelling-assisted comparison of reactor schemes for carbon dioxide removal by enhanced weathering of minerals using seawater. *Chem. Eng. J.* 461, 141804.
- Zwietering, T.N., 1958. Suspending of solid particles in liquid by agitators. *Chem. Eng. Sci.* 8 (3–4), 244–253.